IEEE Access
Multidisciplinary | Rapid Review | Open Access Journal

Received 28 December 2023, accepted 1 February 2024, date of publication 5 February 2024, date of current version 13 February 2024.

Digital Object Identifier 10.1109/ACCESS.2024.3362231

RESEARCH ARTICLE

Energy Management Optimization and Validation of a Hydrogen Fuel Cell-Powered Agricultural Tractor Based on Hierarchical Dynamic Programming

YANYING LI[1], (Member, IEEE), MENGNAN LIU[1,2,3], (Member, IEEE), YITING WANG[1], LIYOU XU[1,2], (Member, IEEE), AND SHENGHUI LEI[1]

[1]College of Vehicle and Traffic Engineering, Henan University of Science and Technology, Luoyang 471003, China
[2]State Key Laboratory of Intelligent Agricultural Power Equipment, Luoyang 471039, China
[3]First Tractor Company Ltd., Luoyang 471004, China

Corresponding authors: Mengnan Liu (liumengnan27@163.com) and Liyou Xu (xlyou@haust.edu.cn)

This work was supported in part by the National Key Research and Development Program under Grant 2022YFD2001204, in part by the National Agricultural Major Scientific and Technological Project under Grant NK202216010401, in part by the Henan Province Key Science and Technology Special Project under Grant 221100110800, in part by the China Machinery Industry Group Company Ltd., and in part by the Youth Science and Technology Fund under Grant QNJJ-PY-2022-14.

ABSTRACT In addressing challenges associated with the constrained enhancement of range performance in pure electric tractors, the difficulty in achieving genuinely eco-friendly agricultural machinery with hybrid powertrains, and the outdated approaches to energy optimization in hydrogen fuel cell tractors, a comprehensive methodology covering the entire spectrum of system design, optimization, and validation is presented. This method constructs an integrated electromechanical and hydraulic power bond graph model for an agricultural tractor, encompassing energy systems, drive systems, and lifting systems. It achieves rapid interaction between 20-sim software and Matlab/Simulink software through a script toolbox. In order to tackle the real-time applicability challenges of dynamic programming, a hierarchical dynamic programming is proposed. The dynamic programming strategy results serve as the upper-level output. At the lower layer, preprocessing of impact value variables is carried out to filter the input variables for the general regression neural network. This enables the real-time application of the dynamic programming algorithm and significantly reduces training time. Finally, validation is conducted through both model-in-the-loop and hardware-in-the-loop. The results demonstrate the correctness and superiority of the designed tractor simulation model and energy management strategy model compared to the power-following strategy. Specifically, in plowing conditions, the dynamic programming and hierarchical dynamic programming strategies exhibited reductions of 10.278% and 6.728%, respectively, in equivalent hydrogen consumption compared to power-following strategy. In transportation conditions, the reductions are 16.02% for dynamic programming strategy and 4.87% for hierarchical dynamic programming strategy, both relative to power-following strategy. This study lays the theoretical groundwork for modeling dynamic systems of tractors and optimizing energy management.

INDEX TERMS Hydrogen fuel cell tractors, bond graph, energy management strategy, model-in-the-loop, hard-ware-in-the-loop.

I. INTRODUCTION

As the foundation of modern agricultural development, agricultural machinery is advancing towards electrification,

The associate editor coordinating the review of this manuscript and approving it for publication was Ayaz Ahmad.

intelligence, and environmental sustainability [1]. Among these, general-purpose tractors, celebrated for their versatility and consistently high annual utilization, stand at the heart of agricultural machinery. The rapid evolution of energy and electric drive technologies is opening up new avenues for the development of highly efficient and eco-friendly tractors [2].

Traditional tractors, which rely solely on diesel engines as their exclusive energy source, present formidable challenges when it comes to addressing issues related to energy deficiency and pollution emissions. In contrast, new energy tractors, equipped with cutting-edge energy systems, offer a viable solution to mitigate environmental pressures. Based on the type of energy source employed, new energy tractors can be classified into three categories: electric tractors, hybrid tractors, and hydrogen fuel cell tractors (HFCTs).

Due to the heavy loads and variable working conditions in agricultural operations, the advancement of pure electric tractor endurance performance is hindered by limitations in battery technology [3]. Although hybrid tractors offer a certain level of protection for the longevity of power batteries [4], [5], [6], their utilization of diesel engines as part of the energy system makes it challenging to achieve the goal of zero pollution emissions. Fuel cells (FCs) offer a host of advantages, including being clean, highly efficient, emission-free, and having a high energy density. As a result, they have emerged as one of the most promising sources of energy in the realm of new energy [7]. However, due to their slower dynamic response and lower power density, FCs are typically combined with other energy units such as battery and supercapacitors to form the energy system of the HFCT. Xu et al. [8] using FC/battery/supercapacitor as the energy system, Sun et al. [9] using fuel cell/supercapacitor as the energy system, and Quan et al. [10] using FC/battery as the energy system, designed the HFCT respectively. A comprehensive comparative analysis reveals that supercapacitors indeed offer advantages in terms of high discharge efficiency and an extended lifespan. However, they are constrained by limited energy storage capacity and are known to exhibit notable voltage fluctuations during discharge, which can pose significant challenges in terms of control. The integration of FCs/ batteries/ supercapacitors serves as an effective strategy to mitigate the drawbacks associated with diverse energy sources. Nevertheless, in the context of tractor operations characterized by frequent load fluctuations and the influence of ground reaction forces on the front and rear wheels, which can have a direct impacts tractor safety, this emphasizes the critical need for a well-thought-out layout of these energy devices. Conversely, batteries stand out due to their swift dynamic response, high power density, and versatile applicability. They effectively address the limitations of FCs while satisfying the tractor's load requirements. Moreover, they offer a straightforward structure that is both easy to control and implement.

Energy management strategies (EMSs) form the foundation of control system development for new energy tractors, and they can be divided into three main categories [11]: rule-based, optimization-based, and intelligent-based. Several scholars have delved into optimization-based and intelligent-based research for pure electric and hybrid electric tractors. LEE et al. [12] optimized power distribution in parallel hybrid tractors using dynamic programming (DP) algorithms, yielding significant results. Meanwhile, Li et al. [13] proposed an enhanced DP algorithm for pure electric tractors, demonstrating superior optimization effects across three load conditions, resulting in an 18% reduction in total energy consumption. However, regarding the HFCT with fuel cell/ battery topologies, Wang [14] designed a power-following (PF) strategy. Compared to traditional tractors, this strategy resulted in a 21.8% improvement in fuel economy. Additionally, Yang et al. [15] proposed an optimization-based EMS that combines temperature control, PF and fuzzy logic control strategies. Utilized a taboo search algorithm was utilized to enhance overall system efficiency. Martini et al. [16] proposed a reference velocity control strategy and evaluated the current reference commands of the converter using power request functions. In comparison to traditional tractors, this approach effectively reduces carbon emissions. Xu et al. [17] introduced an EMS based on fuzzy control, resulting in a reduction in equivalent hydro-gen consumption when compared to CS/CD control strategies. Liu et al. [18] presented an EMS that utilized a multi-objective genetic algorithm. In contrast to PF strategy, it resulted in notably higher remaining state of charge (SOC) levels, with an increase of approximately 11.22% and 6.1% higher, respectively. Moreover, the theoretical hydro-gen fuel consumption saw reductions of approximately 26.49% and 36.21%.

Based on the above research, it can be observed that for the HFCT with FC and battery as energy system, most optimization methods are still using rule-based EMSs that rely on expert experience. There is a dearth of optimization-based and intelligence-based EMSs that offer robust control accuracy and high stability. Furthermore, a comprehensive electromechanical-hydraulic integrated dynamic model of the tractor powertrain has not been developed specifically for the topologies of FC and battery systems.

Therefore, the principal aim of this study is to develop a methodology for configuring parameters, optimizing energy utilization, and simulating a single-motor drive system tailored for the dynamic operational demands of the HFCT. The main tasks to achieve this goal are outlined as follows:

(1) For the designed HFCT with an energy system comprising FCs and batteries, a comprehensive electromechanical-hydraulic integrated power bond graph model (BGM) is constructed, encompassing the tractor's power system, drive system, and lifting system.

(2) To address the current gap in the field of EMS for the HFCT, a hierarchical dynamic programming (HDP) algorithm is designed.

(3) A Matlab-HIL test platform is established, enabling the validation of the designed power system and EMS

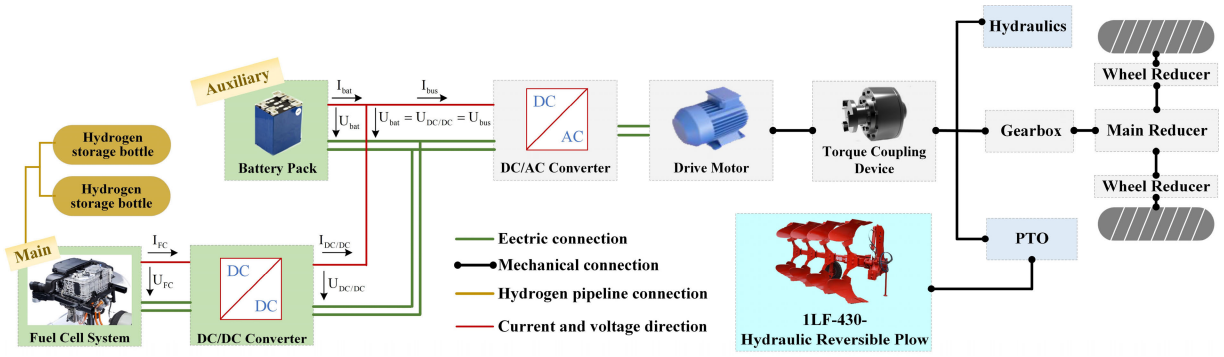

FIGURE 1. Schematic diagram of power system for the hydrogen fuel cell tractor (HFCT).

through both model-in-the-loop (MIL) and hardware-in-the-loop (HIL) simulations, confirming their correctness and superiority.

This research offers theoretical backing for developing the tractor model and optimizing the energy system of the HFCT that utilize both FCs and batteries as their energy sources.

II. DYNAMICAL MODEL

A. SCHEME DESIGN

The comprehensive structure of the designed power system for the HFCT is illustrated in Figure 1. Irregular road surfaces result in the load exhibiting time-varying characteristics, which in turn induce high-frequency motor fluctuations during plowing operations. Therefore, the power supply system needs to not only operate continuously for an extended period but also provide instantaneous peak power. FC offer high energy density. However, they cannot maintain a stable output voltage or current. Therefore, FCs are employed as the primary power source to provide steady-state loads. To regulate the output power and stabilize the output voltage, the FC system is coupled with a unidirectional boost-type DC/DC converter in a serial arrangement. Simultaneously, to compensate for soft output characteristics of the FC system, a battery pack in parallel with the DC bus. This setup is designed to reach the instantaneously high power requirements of the drive motor [19].

B. POWER BOND GRAPH OF ENERGY SYSTEM

1) FUEL CELL MODEL

In this paper, a commercial FC rated at 75kW is chosen and paired with two hydrogen tanks. The related parameters of the FC are shown in Table 1.

The FC stack stands as a pivotal element within the FC system. Hydrogen undergoes disintegration into protons and electrons within the catalytic layer of the anode. Protons navigate the proton exchange membrane, converging with oxygen molecules to produce water, while electrons follow through the external circuit to power the load [20]. The chemical reactions occurring within the fuel cell stack can

TABLE 1. Fuel cell (FC) properties.

System	Parameters	Unit	Value
PEMFC	Nominal voltage	V	0.6
	Rated power	kW	75
	Power density	W/kg	600
	Operating temperature	$^{\circ}C$	40

be delineated as follows:

$$\begin{cases} \text{Anode: } H_2 \rightarrow 2e^- + 2H^+ \\ \text{Cathode: } 2e^- + 2H^+ + \dfrac{1}{2}O_2 \rightarrow H_2O \\ \text{General formula : } \dfrac{1}{2}O_2 + H_2 \rightarrow H_2O \end{cases} \tag{1}$$

PEMFC possesses advantages such as high-power density and strong temperature tolerance. The equivalent circuit diagram is illustrated in Figure 2 [21]. Among them, E_{Nernst} is the thermodynamic electromotive force of the PEMFC, V; R_{act} is internal resistance of activated polarization, Ω; R_{con} is internal resistance of concentration polarization, Ω; R_{ohm} is ohmic polarization resistance, Ω; E_{cell} is the terminal voltage of the PEMFC, V.

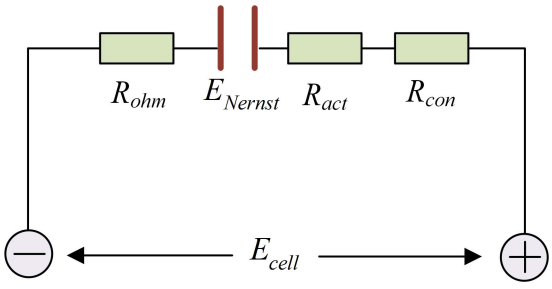

FIGURE 2. The equivalent circuit diagram of single FC.

The operational process of a FC entails the electrochemical transformation of the chemical energy stored in the fuel into electrical energy. When operating under conditions of constant temperature and pressure, the upper limit of electrical power that a FC can achieve is dictated by the negative value

of the change in Gibbs free energy, denoted as [22]:

$$W_{elec} = -\Delta G \tag{2}$$

where ΔG represents the change in Gibbs free energy; W_{elec} represents the electrical work output of the FC, $kW \cdot h$.

The electrical power generated by a FC is the result of multiplying the voltage difference between the anode and cathode by the transferred charge. Given that electrons carry the charge, the electrical work output of the FC can be succinctly represented as follows:

$$W_{elec} = -nFE \tag{3}$$

where n is the number of free electrons, $n = 2$; F is Faraday's constant, $F = 96485.3383C/mol$; E is the voltage difference between the anode and cathode, V.

Combining the two equations mentioned above, the relationship can be expressed as follows:

$$\Delta G = -nFE \tag{4}$$

The Gibbs free energy change for a hydrogen-oxygen FC under standard conditions is $\Delta G^0 = -237kJ/mol$ Therefore, the reversible cell voltage under standard conditions is:

$$E^0 = -\frac{\Delta G^0}{nF} = 1.229V \tag{5}$$

In automotive environments, FC typically operate under non-standard conditions, experiencing pressures ranging from 3 to 5 atmospheres and cell temperatures between $60 \sim 80°C$.Consequently, a modification is essential for the reversible cell voltage in the equation. This modification establishes a comprehensive relationship between voltage, substance concentrations, gas pressures, and temperature, encapsulated in the Nernst equation:

$$E_{Nernst} = \frac{1}{2F}[\Delta G - \Delta S(T - T_0) + RT(\ln P_{H_2} + \frac{\ln P_{O_2}}{2})] \tag{6}$$

where ΔS represents the standard molar entropy change, $J/mol/K$; T is the operating temperature of the FC stack; T_0 is the temperature under standard conditions; R is the gas constant; P_{H_2} and P_{O_2} are the partial pressures of hydrogen and oxygen, respectively.

Combining the dynamic characteristics of a FC, In steady state, a single PEMFC can be expressed as follows:

$$\begin{cases} E_{cell} = E_{Nernst} - U_{act} - U_{conc} - U_{ohm} \\ U_{act} = \varepsilon_1 + \varepsilon_2 T + \varepsilon_3 T \ln(Co_2) + \varepsilon_4 T \ln(i_{fc}) \\ U_{conc} = b \ln(1 - \frac{i}{i_{\lim}}) \\ U_{ohm} = i_{fc} R_{ohm} \end{cases} \tag{7}$$

where U_{act} is the activation polarization loss voltage, V; U_{conc} is the concentration polarization loss voltage, V; U_{ohm} is the ohmic polarization loss voltage, V; $\varepsilon_1 \sim \varepsilon_4$ is a semi-empirical coefficient derived from principles in electrochemistry, thermodynamics, and fluid dynamics; Co_2 denotes the oxygen concentration within the cathodic catalytic layer, mol/cm^3; b is an empirical coefficient; i is electric current density, A/cm^3; i_{fc} is the current of the fuel cell stack, A; T is the system operating temperature; $i_{\lim}$ is limited current, A.

The effective output voltage of the FC is as follows:

$$V_{\text{fc}} = N_{fc} \cdot E_{cell} \tag{8}$$

where V_{fc} represents the actual output voltage of the FC, V; N_{fc} represents the quantity of the FC in series.

The FC output power is as follows:

$$P_{fc} = V_{fc} \cdot i_{fc} \tag{9}$$

where P_{fc} is the output power, kW.

The efficiency is as follows:

$$\eta_{\text{fc}} = \frac{V_{fc}}{N_{fc} \cdot E_{Nernst}} \tag{10}$$

where η_{fc} represents the efficiency.

Combining the empirical formula for polarization voltage mentioned above and the fundamental principles for constructing BG [23], the BGM for the FC is depicted in Figure 3.

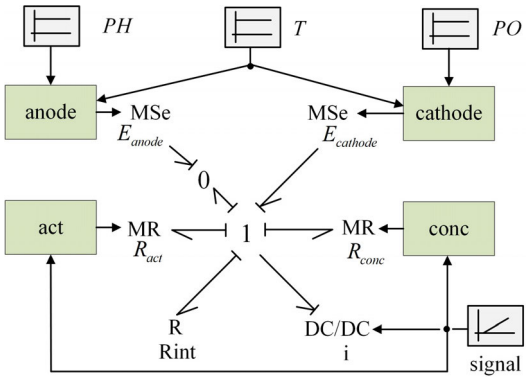

FIGURE 3. Bond graph model for the FC.

The curve depicting the relationship between "Current" and "Voltage" is illustrated in Figure 4. Considering that

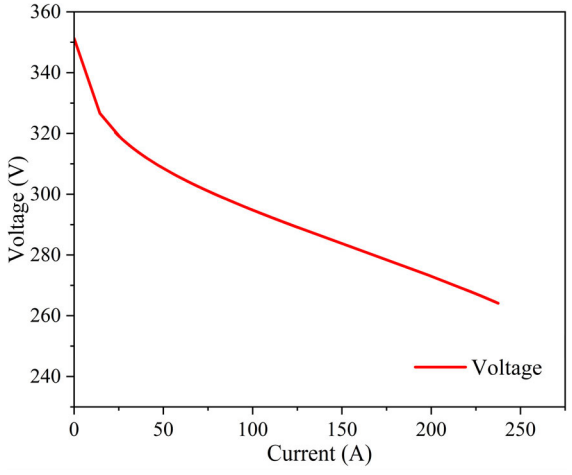

FIGURE 4. Current-Voltage curve of FC system.

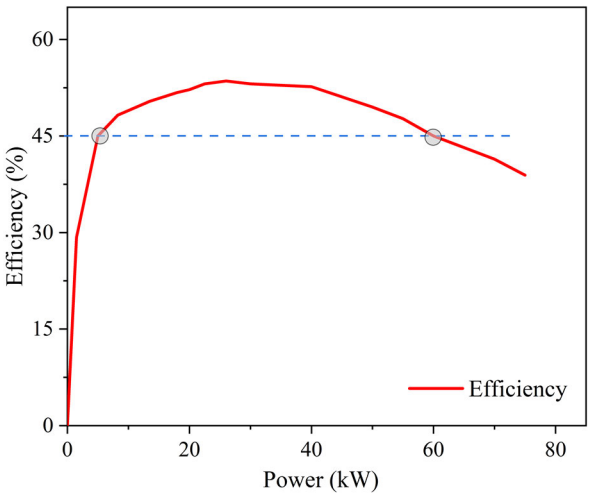

FIGURE 5. Efficiency curve of FC system.

the electrical power consumption by the auxiliary system of a FC typically constitutes 10-20% of the power output from the FC stack, its impact on system efficiency cannot be overlooked. Consequently, when accounting for the auxiliary system consumption, the efficiency curve of the FC system is presented in Figure 5.

2) BATTERY MODEL

The battery model described in this paper uses a first-order RC model, and the equivalent circuit is shown in Figure 6 [23]. The relevant parameters are listed in Table 2. In this figure, U_{Batt} is the terminal voltage, V; I_{Batt} is the output current, A; R_{Batt} is Ohmic resistance, Ω. U_{ocv} is the open circuit voltage, V.

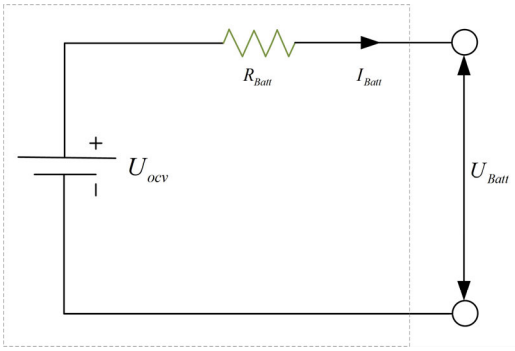

FIGURE 6. The diagram of equivalent circuit for battery.

TABLE 2. Battery properties.

System	Parameters	Unit	Value
Battery	Nominal voltage	V	320
	Nominal charge	Ah	60
	Internal resistance	ohm	0.8

According to the equivalent circuit, the output current of the lithium battery is as follows:

$$I_{Batt} = \frac{U_{ocv} - \sqrt{U_{ocv}^2 - 4 \cdot R_{Batt} \cdot P_{Batt}}}{2 \cdot R_{Batt}} \tag{11}$$

The SOC at the next moment is as follows:

$$SOC(k+1) = SOC(k) - \frac{U_{ocv} - \sqrt{U_{ocv}^2 - 4R_{Batt}P_{Batt}(k)}}{2R_{Batt}Q_{Batt}}\Delta t \tag{12}$$

Utilizing the general method of BGM, the BGM of the battery can be obtained, as shown in Figure 7. The potential source "Se" in the BGM can be utilized to represent U_{ocv}. Due to the negligible temperature variations observed in practical experiments, the adjustable resistor element "MR" is employed to denote the internal resistance of the battery, with the temperature changes being disregarded. The "SOC" in the diagram signifies the battery's state of charge, which is utilized for adjusting control strategies and the SOC signal of the battery. The terms "voltage and current" represent the ports connecting external loads, supplying voltage and energy to the outside, with the current value being feedback from the load.

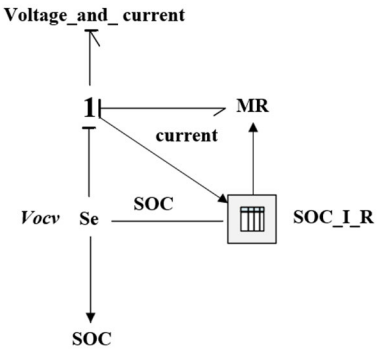

FIGURE 7. The BGM of battery.

C. POWER BOND GRAPH OF DYNAMICAL SYSTEM

Tractors, as off-road machinery, play a crucial role in agricultural activities, encompassing tasks such as plowing, planting, and harvesting. Establishing an integrated model that includes agricultural machinery aids in accurately analyzing agricultural operation levels. The BGM enables cross-physical system modeling. 20-sim provides an interactive, object-oriented modeling and simulation platform [24], [25]. Combined with the specific parameters mentioned above, utilizing the 20-sim software, facilitates the automated modeling of the electromechanical-hydraulic integrated engineering system of the agricultural tractor.

Following the general principles of BGM, establish a power flow diagram model for the HFCT that includes the energy system, drive system, and lifting system. The modeling assumes that the system operates at a constant temperature and has reached a steady state. The meanings of

TABLE 3. The meanings of the nine basic components.

Primary element	Meaning	Equations without causation	Primary element	Meaning	Equations without causation
R	Ohmic component	$e - rf = 0$	MS_f	Modulated current source	$f = f(input)$
I	Inertial element	$e - i\frac{df}{dt} = 0$	1 junction	Flow equality	$\sum e_i = 0$
C	Capacitive element	$f - c\frac{de}{dt} = 0$	0 junction	Potential equality	$\sum f_i = 0$
S_e	Potential source	$e = \text{constant}$	TF	Transverter	$e_1 = re_2, f_2 = rf_1$
MS_e	Modulation potential source	$e = e(input)$	GY	Gyrator	$e_1 = rf_2, e_2 = rf_1$

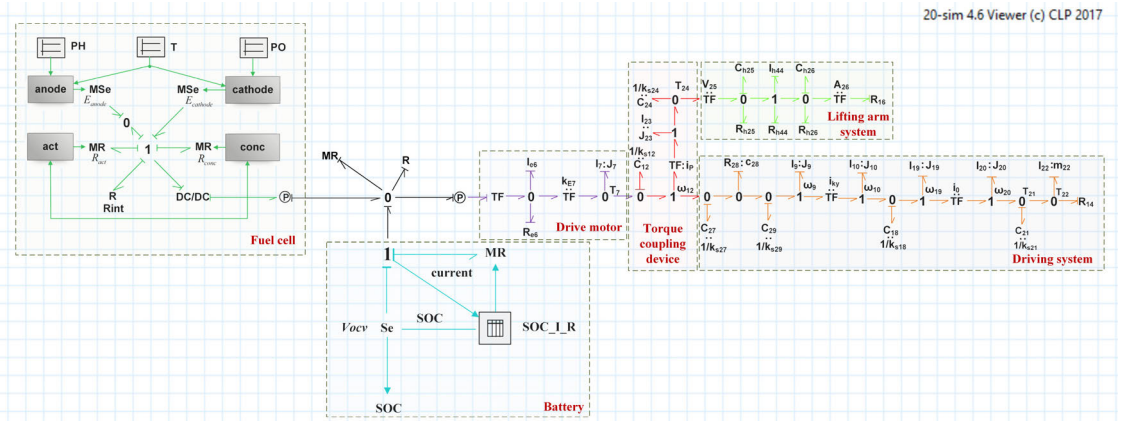

FIGURE 8. The implementation of the bond graph model in 20-sim software.

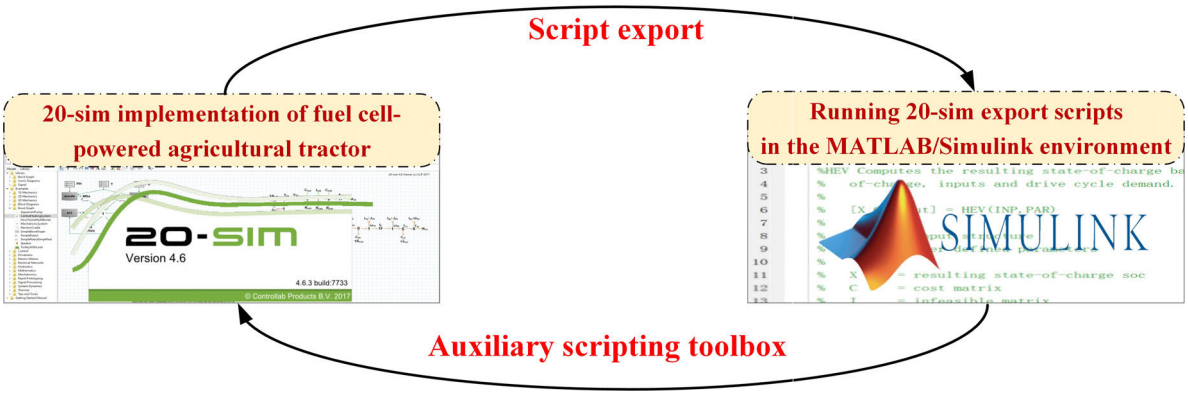

FIGURE 9. The interaction process of Matlab/Simulink and 20-sim.

the nine basic elements are presented in Table 3. The BGM constructed using the BGM software 20-sim is illustrated in Figure 8.

The automation of modeling is achieved with the help of the 20-sim script toolbox, which can automatically recognize and execute matrix scripts that are exported from the 20-sim environment and can be used within the Matlab environment. This eliminates the necessity of manually deriving state equations and significantly reduces modeling time [26]. The rapid interaction process between Matlab/Simulink and 20-sim is il-lustrated in Figure 9.

D. PERFORMANCE VERIFICATION

Based on the original model YTO-LX1000 with rated power of 75 kW, it is paired with the 1LF-430 plow, and the main parameters as listed in Table 4:

In the Matlab/Simulink environment, the correctness of the model construction is verified based on the BGM exported from 20-sim, by assessing the tractor's traction characteristics and dynamic response characteristics.

The traction characteristics analysis is performed under the following conditions: ① Gear transmission efficiency is assumed to be 99%, and friction transmission efficiency

TABLE 4. Tractor properties.

System	Parameters	Unit	Value
Vehicle	Length× width× height	mm	4330×2160×2865
	Wheel base	mm	2100
	Curb weight	kg	3180
	Driving wheel radius	m	0.381
Plow implement	Model	-	1LF-430
	Share number	-	4
	Single plowshare width	cm	25
	Soil specific resistance	kN/cm^2	5
Motor	Rated speed	r/min	3000
	Nominal voltage	V	320
	Rated power	kW	75
Drivetrain	Ploughing gear ratio	-	1.95
	Transport gear ratio	-	1.25

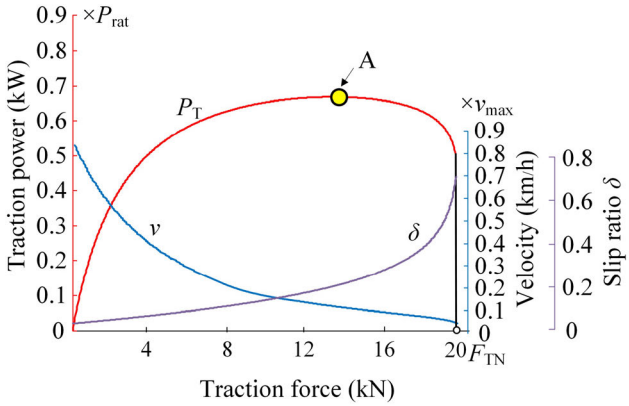

FIGURE 10. The traction characteristics of the HFCT.

is 96%; ② According to reference [27], it is indicated that the transmission efficiency of a tractor utilizing a continuously variable hydraulic transmission using volume control is significantly affected by the transmission ratio, ranging from 0.7 to 0.99. The mean value is taken for analysis; ③ the ratio of driving resistance to rated traction force is 0.87. Figure 10 depicts the tractor's traction characteristics. In the figure, P_{rat} is the motor's rated power, kW; $v_{\max}$ is the maximum speed during plowing operations. As the traction force rises, so does the traction power, edging closer to the ideal external characteristic. Point A represents the maximum traction power point. As the traction force increases, the slip rate also rises.

When analyzing the dynamic characteristics, a unit angular displacement step signal is applied, and the inertia element's inertia, the amplitude of the angular dis-placement step response function, and system sensitivity are normalized. The step response characteristics of the tractor's driving wheel are shown in Figure 11. In comparison to a certain model of YTO-tractor with the same power, the designed tractor exhibits smoother operation, shorter stabilization time, and better responsiveness.

In summary, the traction characteristics meet the design requirements, and the established dynamic model is accurate. The dynamic response characteristic is superior to that of a YTO tractor with the same power, and the driving wheel exhibits superb dynamic responsiveness.

III. ENERGY MANAGEMENT STRATEGY

The EMS for a HFCT with the FC/battery energy system is a multidimensional, nonlinear, constrained, and finite-time domain optimization problem [28]. In practical systems where a FC is linked in series with a DC/DC converter, the output power of the FC is effectively managed by the DC/DC unit, which is typically regulated by control-ling the current. This means that the actual output power of the FC is contingent on the power delivered at the output of the DC/DC converter.

A. DYNAMIC PROGRAMMING

Dynamic programming, by transforming multi-stage decisions into a series of single-stage optimal decisions enables the attainment of global optimal control for the system, provided that complete operating condition information is available. This approach proves to be particularly suitable for conducting research on EMSs for the HFCT. Adhering to Bell-man's principle, which states that irrespective of the starting state and initial choice, subsequent decisions should collectively form the optimal decision [29]. The schematic diagram for the solution of DP is shown in Figure 12, where x_k is the set of all discrete state points at time k; x_k^i the i-th discrete state point at time k; $arc\_\cos t(x_k^{i\to j})$ is the arc-cost from the i-th state point at time k to the j-th state point at time $(k+1)$; J_temp(x_k) is the temporary cost function for each point at time k; J_cost_to_go(x_k) is the optimal cost function for each point at time k.

1) PROBLEM FORMULATION

In this paper, the state variable is the SOC and the control variable is the output power of the DC/DC converter. Therefore, in discrete-time, the general form of the state equation is typically as follows:

$$\begin{cases} x(k+1) = f(x(k), u(k)) \\ x = SOC \\ u = P_{DC/DC} \end{cases} \tag{13}$$

where x is the state variable; k is the discretization computation step size; u is the control variable. $P_{DC/DC}$ is the output power of the DC/DC converter, kW.

The power equilibrium equation is as follows:

$$\frac{P_{\text{load}}}{\eta_{DC/AC}} = P_{DC/DC} + P_{Batt} \tag{14}$$

where $\eta_{DC/AC}$ is the efficiency of the DC/AC converter, set to constant; P_{load} is the motor demand power, kW.

Combining Equation (12). and Equation (14), the equation describing the transition of the system's state is

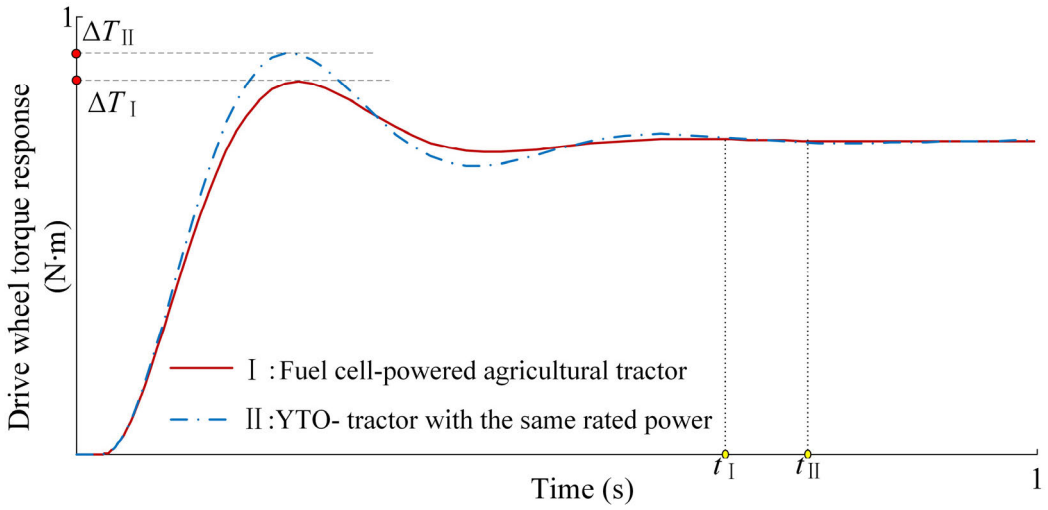

FIGURE 11. Dynamic response characteristics of the HFCT.

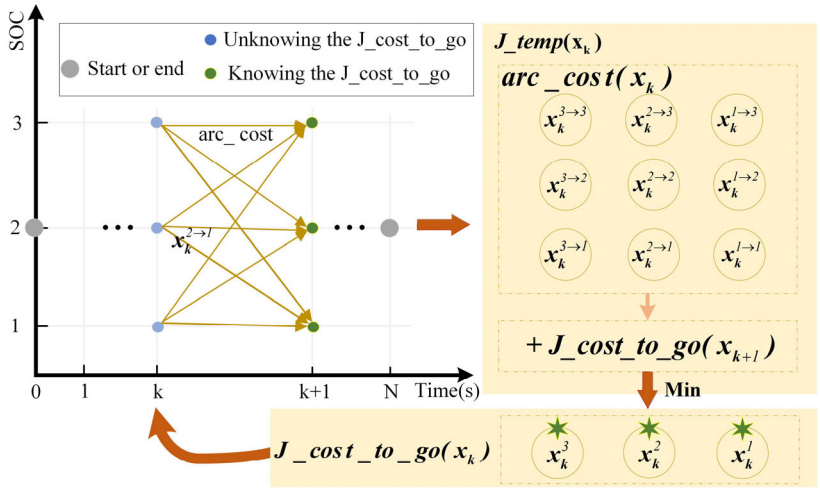

FIGURE 12. Schematic diagram for the solution of DP.

as follows:

$$SOC(k+1) = SOC(k) - \frac{U_{ocv}}{2R_{Batt}Q_{Batt}} \cdot \Delta t + \frac{\sqrt{U_{ocv}^2 - 4R_{Batt}(P_{load}/\eta_{DC/AC} - P_{DC/DC})}}{2R_{Batt}Q_{Batt}} \cdot \Delta t \quad (15)$$

where $\Delta t = 1s$ indicates the sampling interval.

The overall hydrogen consumption is selected as the objective function:

$$J = \min \sum_{k=1}^{N} L[x(k), u(k)] = \sum_{k=1}^{N} J_{H_2}(k) \quad (16)$$

$$J_{H_2}(k) = C_{fc}(k) + \mu C_{Batt}(k) \quad (17)$$

where $C_{fc}(k)$ is FC hydrogen consumption, g/s. $C_{Batt}(k)$ is the equivalent hydrogen consumption of the battery, g/s. μ is the penalty coefficient. Due to SOC that is too high or too low will reduce the charge and discharge efficiency, SOC should be maintained in a relatively stable state. Therefore, the concept of penalty function for SOC is introduced to correct SOC [30]:

$$\mu = 1 - 2\beta \frac{SOC(k) - 0.5(SOC_{\max} + SOC_{\min})}{SOC_{\max} - SOC_{\min}} \quad (18)$$

where β is the adjustment coefficient, $\beta = 0.4$; $SOC_{\max}$ and $SOC_{\min}$ are the upper and lower bounds of SOC.

Based on the FC model shown in Figure 2, hydrogen consumption of the FC can be acquired as follows:

$$C_{fc}(k) = \frac{1}{LHV} \int \frac{P_{fc}(k)}{\eta_{fc}(k)} dt \quad (19)$$

where LHV stands for the low calorific value of hydrogen, $LHV = 120MJ/kg$. η_{fc} represent the FC's output efficiency.

During operation, the battery of the non-plug-in tractor described in this paper exclusively relies on the consumption of hydrogen by the FC for its energy. Therefore, the variation of SOC can be considered equivalent to the consumption of hydrogen. An expression for the instantaneous equivalent hydrogen consumption is established [31]. Equation (20), as shown at the bottom of the page, where C_{Batt_chg} and C_{Batt_dis} are instantaneous equivalent hydrogen consumption of the battery during charging and discharging processes, g/s; C_{fc_avg} is the average hydrogen consumption of the FC, g/s; η_{chg_avg} and η_{dis_avg} represent the average charging and discharging efficiency of the battery, respectively; P_{dc_avg} is the average power of the DC/DC converter; R_{chg} and R_{dis} represent the internal resistance of the battery during charging and discharging, respectively.

In the optimization process, several constraints are imposed to prevent over-charging and over-discharging of the battery, extend its lifespan, and limit the wide-ranging output of the FC to maintain its durability. Additionally, constraints are introduced to protect the FC stack by limiting the maximum power change rate, thereby controlling transient response variations. The specific constraints are as follows:

$$\begin{cases} SOC_{\min} \le SOC \le SOC_{\max} \\ P_{fc\_\min} \le P_{fc} \le P_{fc\_\max} \\ \Delta P_{fc} \le \Delta P_{fc\_\max} \end{cases} \tag{21}$$

where $SOC_{\max} = 0.7$, $SOC_{\min} = 0.5$; $P_{fc\_\min} = 5kW$, $P_{fc\_\max} = 60kW$; $\Delta P_{fc\_\max} = 15kW/s$.

In order to eliminate the points that do not fit the constraints of Equation (16). existing in the discrete points, a penalty term is introduced. This ensures that each control variable in the feasible region is a point within the constraints.

$$Q(k) = \begin{cases} 0 & If\ Eq.(21)\ is\ satisfied \\ inf & If\ Eq.(21)\ is\ \text{not}\ satisfied \end{cases} \tag{22}$$

where $Q(k)$ is the penalty term.

In summary, the objective function is extended as follows:

$$J_{H_2}(k) = C_{fc}(k) + \mu C_{Batt}(k) + Q(k) \tag{23}$$

In order to comprehensively observe the optimization effects of the proposed control strategy, initial and final values for the battery SOC is separately predefined for plowing and transportation conditions, taking into account power requirements and previous experiences:

$$\begin{cases} SOC_{IP} = 70\% \\ SOC_{FP} = 65\% \end{cases}, \quad \begin{cases} SOC_{IT} = 72\% \\ SOC_{FT} = 70\% \end{cases} \tag{24}$$

where SOC_{IP} and SOC_{FP} are the initial and final SOC under plowing conditions; SOC_{IT} and SOC_{FT} are the initial and final SOC under transportation condition.

2) SOLUTION METHODS

Based on the fundamental concept of DP, use the Matlab simulation software to perform offline inverse analysis for determining the optimal control input. Then, input these results into simulation model of the HFCT for forward optimization simulation, yielding the best decision variables and optimal trajectory.

The specific DP algorithm process is shown in the diagram as depicted in Figure 13.

1) Initialization. Research [32] has demonstrated an inverse relationship between the precision of discretization and the value of objective function. Additionally, the impact of the state variable's level of discretization on this function surpasses that of the control variable. Therefore, $\Delta SOC = 0.005$, the discrete grid number M = 60; $\Delta P_{DC/DC} = 2.75$, the discrete grid number T = 20.
2) Reverse solving. As the terminal state values are known at the N-th stage, the implementation process can be divided into three stages: N →(N-1), (N-1)→1, and 1→0. The first and third stages follow the following equation:

$$\begin{aligned} arc\_cost\left(x_{N-1}^{i}\right) &= J\_temp\left(x_{N-1}^{i}\right) \\ &= J\_cost\_to\_go\left(x_{N-1}^{i}\right) \end{aligned} \tag{25}$$

It's important to emphasize that, irrespective of the infinitesimal discretization precision applied to state and control variables, it does not ensure that every point in the space aligns perfectly with the grid points. Linear interpolation serves as the method for determining the optimal cost function by interpolating between data points.

- *If* x_{k+1} *precisely coincides with the grid point* x_{k+1}^{i-1} :

$$\begin{cases} J\_temp\left(x_k^i\right) = arc\_cost\left(x_k^i\right) + J\_\cos t\_to\_go\left(x_{k+1}^{i-1}\right) \\ J\_\cos t\_to\_go\left(x_k^i\right) = \min J\_temp\left(x_k^i\right) \end{cases} \tag{26}$$

$$C_{Batt}(k) = \begin{cases} C_{Batt\_dis}(k) = \dfrac{P_{Batt}(k)}{\eta_{chg\_avg}} \dfrac{C_{fc\_avg}}{P_{dc\_avg}} \left(\dfrac{1}{2} + \dfrac{1}{2}\sqrt{1 - \dfrac{4R_{dis}P_{Batt}}{V_{ocv}^2}}\right)^{-1} P_{Batt} \ge 0 \\ C_{Batt\_chg}(k) = P_{Batt}(k)\eta_{dis\_avg} \dfrac{C_{fc\_avg}}{P_{dc\_avg}} \left(\dfrac{1}{2} + \dfrac{1}{2}\sqrt{1 - \dfrac{4R_{chg}P_{Batt}}{V_{ocv}^2}}\right)^{-1} P_{Batt} < 0 \end{cases} \tag{20}$$

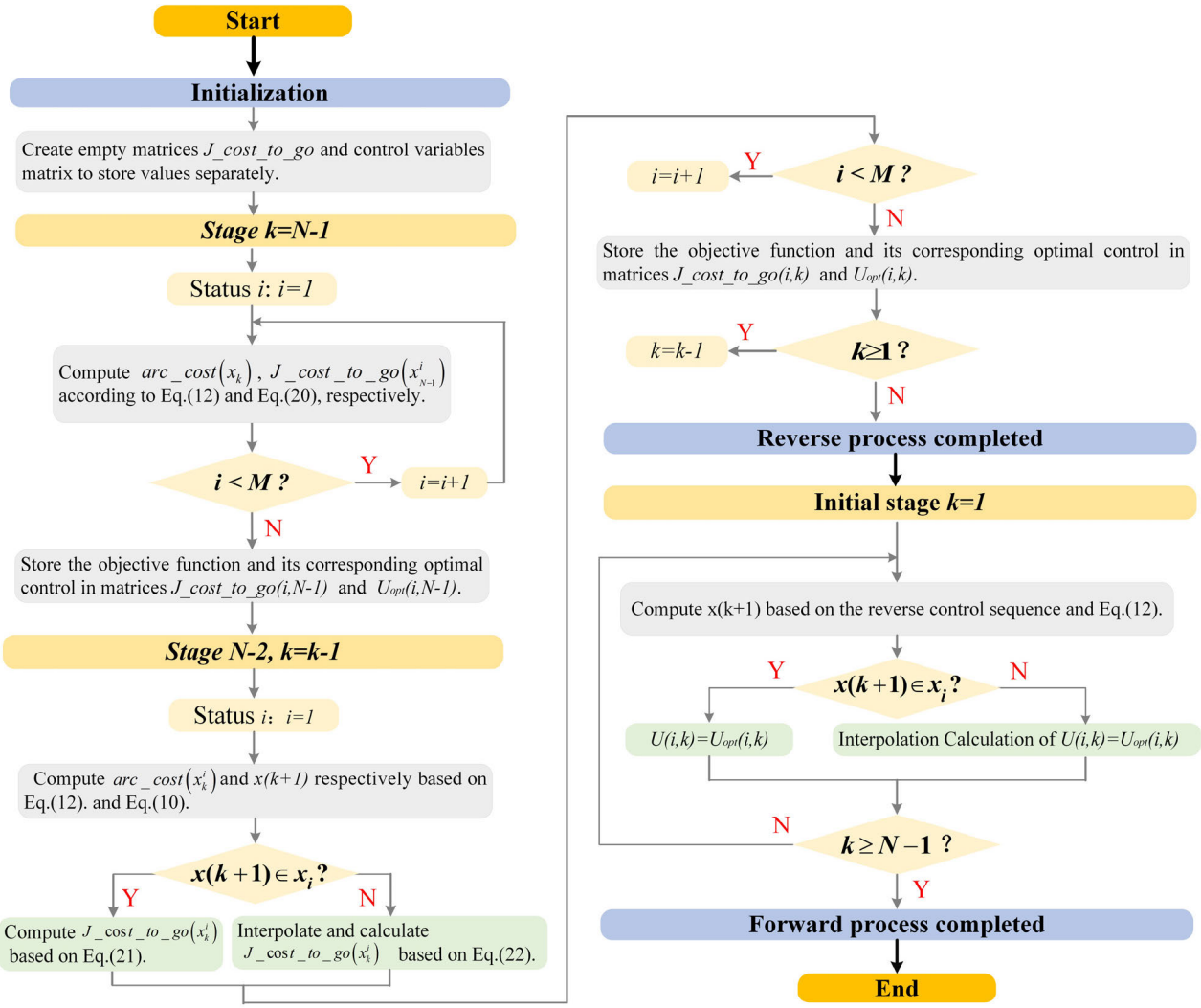

FIGURE 13. The flowchart of DP algorithm.

- *If x_{k+1} does not align with the grid point:*

$$\begin{cases} J\_temp\left(x_k^i\right) = arc\_cost\left(x_k^i\right) + J\_\cos t\_to\_go\left(x_{k+1}^*\right) \\ J\_\cos t\_to\_go\left(x_k^i\right) = \min J\_temp\left(x_k^i\right) \end{cases} \tag{27}$$

where x_k^i, x_{k+1}^{i-1}, x_{k+1}^* are the discrete state variables of interpolation points: i at time k, point $(i\text{-}1)$ at time $(k+1)$ and point interpolation at time $(k+1)$ respectively.

3) Forward optimization. Following the reverse solving process, the optimal objective functions and corresponding control sequences for different states at each stage with respect to the N stages are stored. This prepares the system for forward computation. The optimal decision values are derived through linear interpolation, allowing calculations to proceed up to stage N. As a result, the complete optimal state trajectory and the corresponding optimal control decision sequence are obtained.

B. HIERARCHICAL DYNAMIC PROGRAMMING

The DP algorithm is powerful but not suitable for real-time applications due to its prerequisites. Addressing this issue, a hierarchical dynamic programming (HDP) control strategy is proposed. The upper layer takes the results of a DP as its output. The lower layer, utilizing the general regression neural network (GRNN) algorithm, learns from the upper layer's power allocation results and applies them in real-time. Additionally, the mean impact value (MIV) algorithm is employed to reduce training times caused by large data dimensions, as illustrated in the flowchart in Figure 14.

1) GENERALIZED REGRESSION NEURAL NETWORK

The GRNN exhibits superior learning efficiency and generalization capabilities [33]. It is founded on nonlinear regression

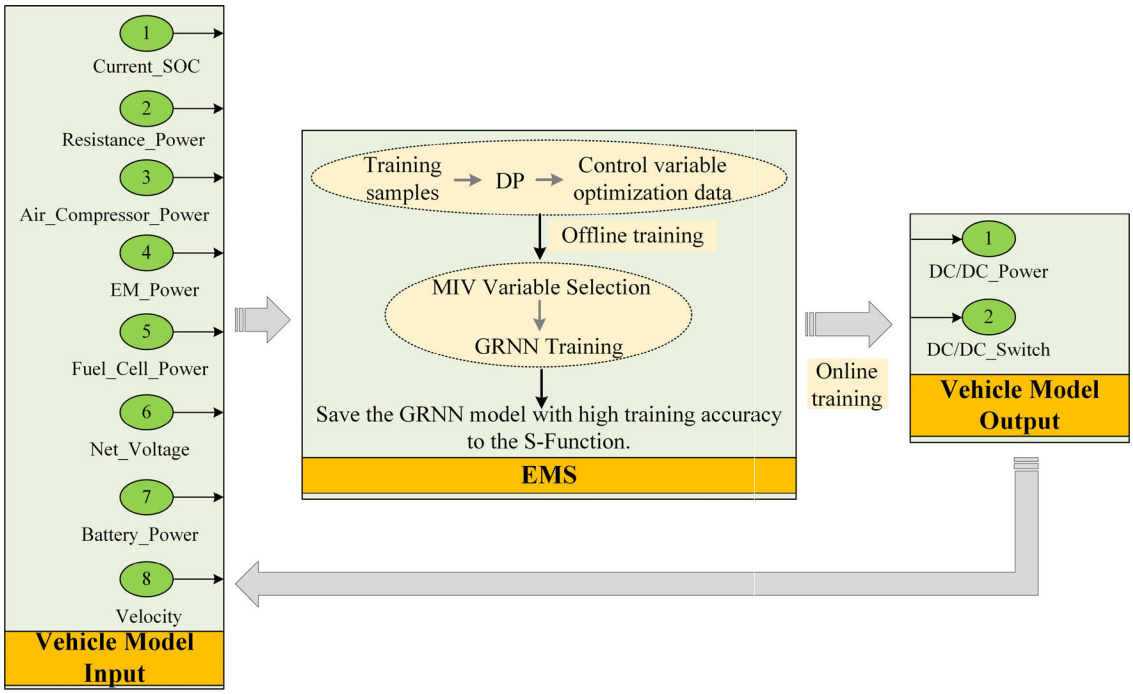

FIGURE 14. The control strategy diagram of hierarchical dynamic programming.

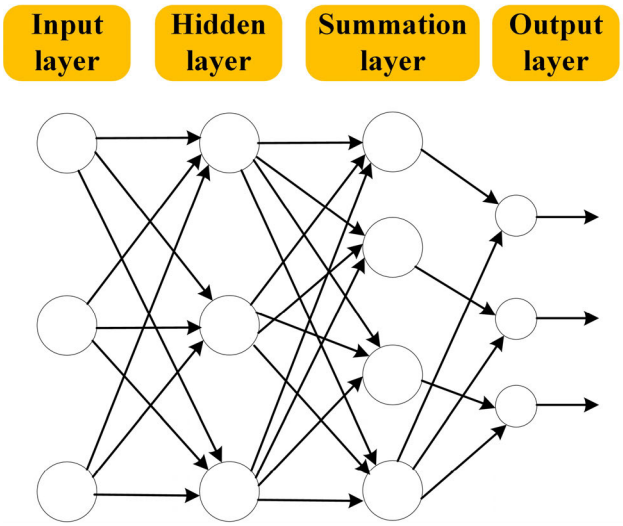

FIGURE 15. The architectural layout of the generalized regression neural network (GRNN).

analysis, rendering it well-suited for ad-dressing nonlinear multi-constraint problems. The architectural layout of the GRNN, as depicted in Figure 15 [34], encompasses four tiers of neurons. Each tier comprises multiple nodes, with interconnections between nodes of different layers established by weighted connections. Conversely, nodes within the same layer remain unconnected.

The optimization process is as follows:

1) Establishing the centers for the radial basis functions within the hidden layer neurons. In this step, data samples are transmitted from the input layer to the hidden layer, with the input matrix denoted as U, and the corresponding output matrix denoted as R:

$$U = \begin{bmatrix} u_{11} & u_{12} & \cdots & u_{1Q} \\ u_{21} & u_{22} & \cdots & u_{2Q} \\ \vdots & \vdots & \ddots & \vdots \\ u_{P1} & u_{P2} & \cdots & u_{PQ} \end{bmatrix},$$
$$R = \begin{bmatrix} r_{11} & r_{12} & \cdots & r_{1Q} \\ r_{21} & r_{22} & \cdots & r_{2Q} \\ \vdots & \vdots & \ddots & \vdots \\ r_{S1} & r_{S2} & \cdots & r_{SQ} \end{bmatrix} \tag{28}$$

where P corresponds to the input variable size; S represents the output variable size; Q stands for the sample count in the training set; u_{ij} denotes the i-th input variable on the j-th samples; t_{ij} denotes the i-th output variable on the j-th sample.

The centers of the radial basis functions for the Q hidden layer neurons are as follows:

$$C = U^R \tag{29}$$

where C is the centers of the radial basis function.

2) Determining the thresholds of hidden layer neurons. The threshold values for the Q neurons in the hidden layer are as follows:

$$b_1 = [b_{11}, b_{12}, \cdots, b_{1Q}]' \tag{30}$$

where b is the threshold;$b_{11} = b_{12} = \cdots = b_{1Q} = 0.8326/spread$, spread is the spreading rate of the radial basis functions.

During the training process, the only parameter that needs adjustment in the GRNN is the smoothing factor, which is the most critical factor determining the size of prediction errors. The smoothing factor denoted as σ, and if σ is too small, it can lead to overfitting, if σ is too large, the errors can become too significant. Therefore, the optimal value of σ is chosen through iterative tuning. The parameter tuning approach is to directly adjust the spreading coefficient of the radial basis functions associated with σ.

3) Determining the weights connecting the hidden layer and the output layer. The output of the hidden layer neurons is:

$$a^i = \exp(-\|C - u_i\|^2 b_1), \quad \mathrm{i} = 1, 2, \cdots, \mathrm{Q} \tag{31}$$

where $p_i = [p_{i1}, p_{i2}, \cdots, p_{iR}]'$ is the i-th training sample vector; a^i is the output of the hidden layer neurons. W is the connection weights in order to train the set output matrix, expressed as follows:

$$W = R \tag{32}$$

4) Calculating the output layer neuron outputs.

When the connection weights are determined, they can be calculated using the normalized dot-product weight function and the linear transfer function. As shown in follows:

$$n_i = \frac{Wa^i}{\sum_{j=1}^{Q} a_j^i}, \quad \mathrm{i} = 1, 2, \cdots, \mathrm{Q} \tag{33}$$

$$y^i = purelin(n^i) = n^i, \quad \mathrm{i} = 1, 2, \cdots, \mathrm{Q} \tag{34}$$

2) PREPROCESSING OF INPUT VARIABLES

In order to mitigate challenges like prolonged training times and unwieldy net-work sizes arising from high-dimensional data, feature dimension reduction techniques are applied to the input variables of neural networks. Commonly used dimension reduction methods encompass principal component analysis, factor analysis, and MIV. Among these, MIV stands out as one of the most effective indicators for evaluating variable relevance within a neural network [35].

The positive and negative signs of MIV represent the direction of influence that independent variables exert on the output variable, while the absolute value signifies the extent of their impact. A common technique involves creating two new training samples by adding and subtracting 10% to the feature indicator values of the independent variables. Then, the change in influence on the output information variable (IV) is calculated for each variable, and the average of these IV values is computed to obtain the MIV value for that specific independent variable. This process is iteratively repeated for each independent variable, resulting in MIV values for all variables. Finally, these MIV values are ranked based on their absolute magnitude. This ranking approach helps in retaining important features from the original data while revealing the essential characteristics of the dataset.

The specific screening process is as follows:

1) Constructing training samples. Initially, the neural network is trained with matrix X as the input and the $P_{DC/DC}$ as the output. Subsequently, two new training samples denoted as $X_i(1), X_i(2)$ are generated by adding and subtracting 10% from the input matrix X.

$$X = \begin{bmatrix} x_{11} & x_{12} & \cdots & x_{1m} \\ x_{21} & x_{22} & \cdots & x_{2m} \\ \vdots & \vdots & \ddots & \vdots \\ x_{n1} & x_{n2} & \cdots & x_{nm} \end{bmatrix} \tag{35}$$

$$X_i(1) = \begin{bmatrix} x_{11} & x_{12} & \cdots & x_{1i} + 10\%x_{1i} & \cdots & x_{1m} \\ x_{21} & x_{22} & \cdots & x_{2i} + 10\%x_{2i} & \cdots & x_{2m} \\ \vdots & \vdots & \ddots & \vdots & \ddots & \vdots \\ x_{n1} & x_{n2} & \cdots & x_{ni} + 10\%x_{ni} & \cdots & x_{nm} \end{bmatrix} \tag{36}$$

$$X_i(2) = \begin{bmatrix} x_{11} & x_{12} & \cdots & x_{1i} - 10\%x_{1i} & \cdots & x_{1m} \\ x_{21} & x_{22} & \cdots & x_{2i} - 10\%x_{2i} & \cdots & x_{2m} \\ \vdots & \vdots & \ddots & \vdots & \ddots & \vdots \\ x_{n1} & x_{n2} & \cdots & x_{ni} - 10\%x_{ni} & \cdots & x_{nm} \end{bmatrix} \tag{37}$$

where m represents the quantity of variables; n represents the quantity of samples each variable contains.

2) Calculating IV The IV of the i-th variable is as follows:

$$IV_i = Y_i(1) - Y_i(2) \tag{38}$$

where $Y_i(1)$ and $Y_i(2)$ is the output value of the i-th variable.

3) Calculating MIV and relative contribution rate.

Using the DP optimization results as training samples, initially, five feature variables are preliminarily selected, including demand power, vehicle speed, power from the previous time step in the battery, power from the previous time step in the FC, and SOC. The MIV and relative contribution rate denoted as are computed for each of these feature variables. Variables with high relative contribution rates are chosen as input variables for the GRNN.

The formula for calculating MIV is as follows:

$$MIV_i = \frac{1}{n}\sum_{j=1}^{n} IV_i(j), \quad \mathrm{i} = 1, 2, \ldots, m \tag{39}$$

Relative contribution rate pertains to the ratio of the impact value of the i-th feature variable to the total sum of MIV values, which is shown as follows:

$$\alpha_i = \frac{|MIV_i|}{\sum_{i=1}^{n} |MIV_i|}, \quad \mathrm{i} = 1, 2, \ldots, 5 \tag{40}$$

4) Evaluating quality.
The quality of the GRNN is assessed by evaluating the mean square error denoted as E and the coefficient of determination denoted as R^2.

$$\begin{cases} E = \dfrac{1}{l}\sum_{i=1}^{l}(\hat{y}_i - y_i)^2 \\ R^2 = \dfrac{(l\sum_{i=1}^{l}\hat{y}_i y_i - \sum_{i=1}^{l}\hat{y}_i \sum_{i=1}^{l} y_i)^2}{(l\sum_{i=1}^{l}\hat{y}_i^2 - (\sum_{i=1}^{l}\hat{y}_i)^2)(l\sum_{i=1}^{l} y_i^2 - (\sum_{i=1}^{l} y_i)^2)} \end{cases} \tag{41}$$

where l is sample size; y_i represents the real output value of the i-th sample; $\hat{y}_i$ represents the predicted value of the neural network for sample i, $i = 1, 2, \ldots, l$.

IV. SIMULATION AND RESULT ANALYSIS

In accordance with the V-shaped rapid development process, the simulation is di-vided into two phases: MIL and HIL. MIL is utilized for the initial validation of the correctness of the HTCT's simulation model and the EMS simulation model. HIL is then employed to bolster model confidence and significantly reduce development time.

In order to enhance the vertical comparability of EMSs, a rule-based PF strategy is chosen as the comparative control strategy. The PF strategy diagram is depicted in Figure 16.

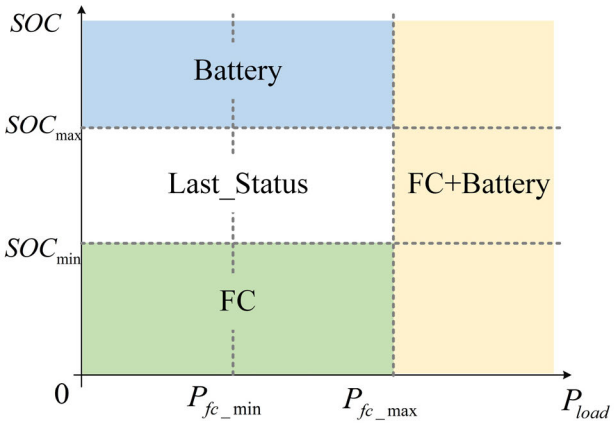

FIGURE 16. The diagram of power-following (PF) strategy.

A. WORKING CONDITION

1) PLOUGHING CONDITION

To ensure an accurate simulation of real-world operations, and in accordance with the parameter selection results for key components, the YTO-1000 tractor produced by the collaborative enterprise YTO Group Corporation, paired with the 1LF-430 bidirectional amplitude-adjustable plow for field tests [36], is selected. The test location is the field test site for all terrain types in Mengjin test base of China YTO Group, and the conditions for the field tests are detailed in Table 5. During the experiment, in the latter 200 seconds, the plowing depth is reduced while simultaneously decreasing the vehicle's speed. This adjustment is made to better observe whether the overall operating status of the tractor under various load conditions aligns with the settings of the EMS. The experimental conditions and the load spectrum for plowing operations are illustrated in Figure 17. The average tractive resistance is 11.23kN.

TABLE 5. Conditions for measuring ploughing resistance.

Time(s)	Velocity(km/h)	Ploughing depth(cm)
0~1000	8	25
1000~1200	6	20

2) TRANSPORTATION CONDITION

The transportation condition is optimized for the suburban cycle condition EUDC_Man at 30% intensity, with a maximum speed of 36 km/h, as illustrated in Figure 18. The tractor is operating under full load with an effective payload of 2340kg.

B. MODEL-IN-THE-LOOP

The MIL approach utilizes the 20-sim simulation software to create the for-ward simulation model for the HFCT. In parallel, the Matlab/Simulink simulation software is employed to develop the EMS simulation model. The simulation software interaction is facilitated through the script toolbox for seamless communication.

Figure 19 and Figure 20 display the variations in the speed when three different EMSs are implemented, respectively. These figures illustrate that the actual speed can basically track the target speed in real-time. These simulation results affirm the precision of the constructed simulation model. Specifically, under plowing conditions, the speeds with the three EMSs fluctuate within an error range of [−0.49, 0.27]. The reason for these tracking fluctuations is attributed to the complex and variable operating conditions of the tractor, leading to a Gaussian-distributed random fluctuation in the traction load during plowing operations. And during transportation conditions, slight fluctuations occur at moments of speed stability, with the remaining periods exhibiting negligible fluctuations below 0.01.

C. HARDWARE-IN-THE-LOOP

HIL simulation involves integrating an actual controller with the vehicle simulation model, resulting in a semi-physical simulation. The simulation platform setup can be seen in Figure 21 and the HIL implementation process is shown in Figure 22. This simulation encompasses both hardware and software components. The hardware includes an HIL cabinet manufactured by the National Instruments company and a specialized vehicle control unit for FC systems called PowerECU-57A, produced by Shan-dong EXP Fuel Cell

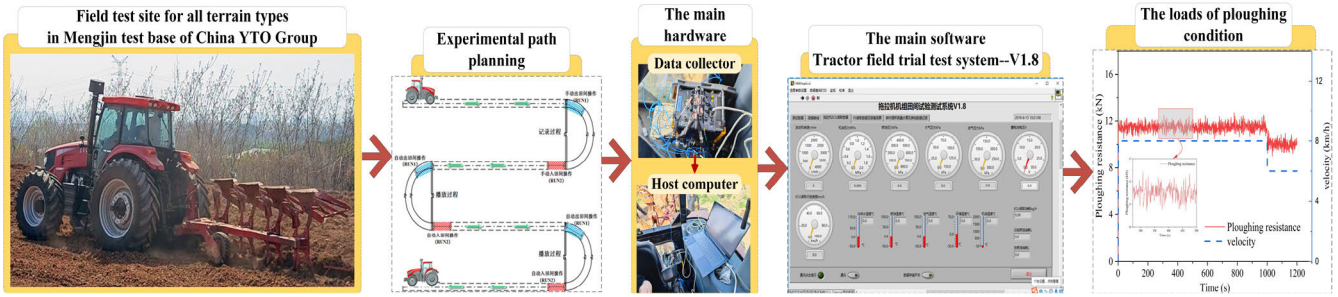

FIGURE 17. The experimental conditions for ploughing.

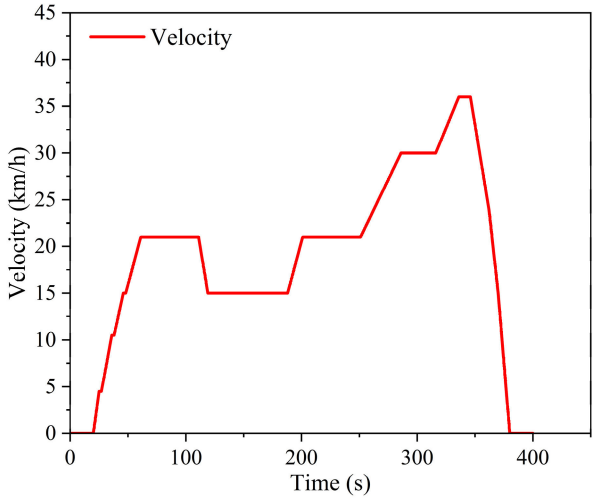

FIGURE 18. Schematic diagram of transportation operating conditions.

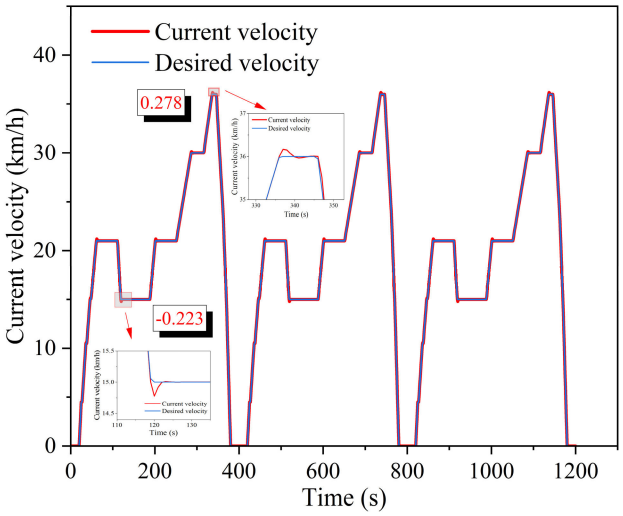

FIGURE 20. Comparison chart between target speed and actual speed under transportation conditions.

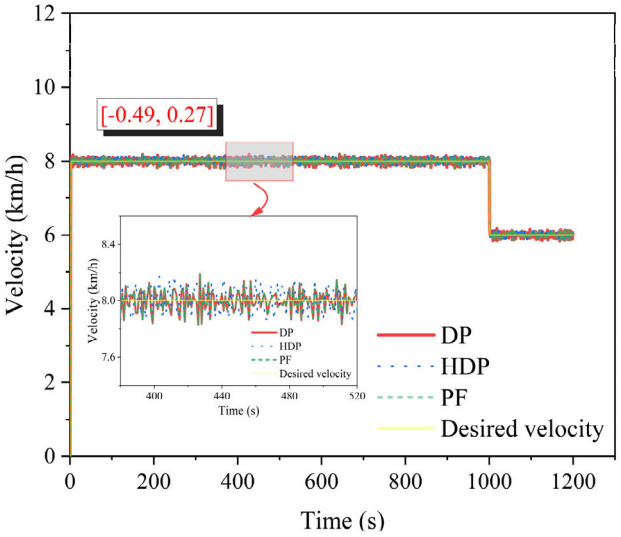

FIGURE 19. Comparison chart between target speed and actual speed under plowing conditions.

Technology Co.,Ltd. The EMS communication interface settings are finetuned using the I/O modules provided by the PowerBSP plug-in software. Utilizing tools like Matlab/RTW code generation and PowerBOOT code loading, C code for the energy management strategy and seamlessly integrate it with the ECU's low-level programming is generated. The compiled vehicle simulation model is then imported into NI VeriStand software and connected to the NI real-time simulator through con-figuration board interfaces. Information exchange between the drive controller and the real-time simulation processor is accomplished via the CAN bus. Online data observation and calibration are performed through PowerCAL in the host computer [37], [38].

D. RESULTS ANALYSIS

1) PLOUGHING CONDITION

Figure 23 displays the power output from various energy sources of the HFCT under three different EMSs. The longitudinal comparison shows that, due to the working conditions and ploughing load settings are the same across these three strategies, the power output from the motor remains consistent. However, there are variations observed in the power output from the FC as follows: DP<HDP<PF. In contrast to the PF strategy, both the DP and HDP strategies demonstrate the ability to maintain a steady output from the FC, with

FIGURE 21. Hardware-in-the-loop test setup diagram.

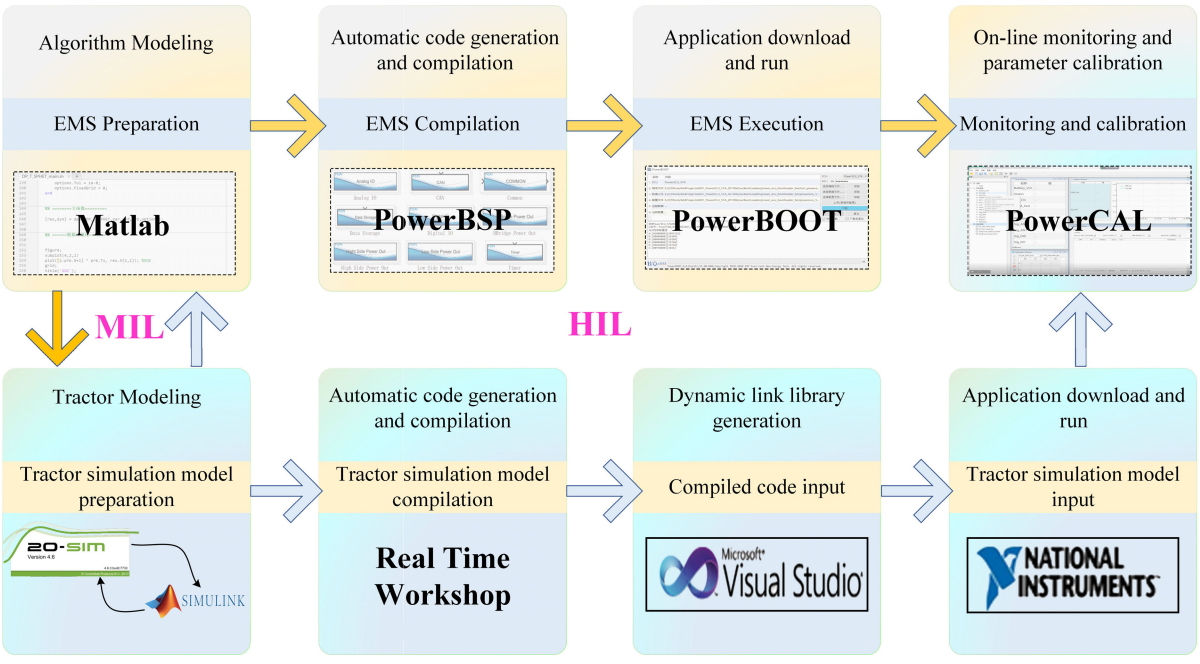

FIGURE 22. The flow chart of implementation process for hardware-in-the-loop test.

peak fluctuation power being supplemented by the battery. Notably, during the initial 6s of operation, both DP and HDP strategies effectively address the output power deficiencies of the FC. Be-yond the 1000s, as the overall load on the vehicle decreases, the FC operates at a higher efficiency region, producing substantial power output. It utilizes this power to charge the battery within the allowable charging rate, thus extending the lifespan of the traction battery pack.

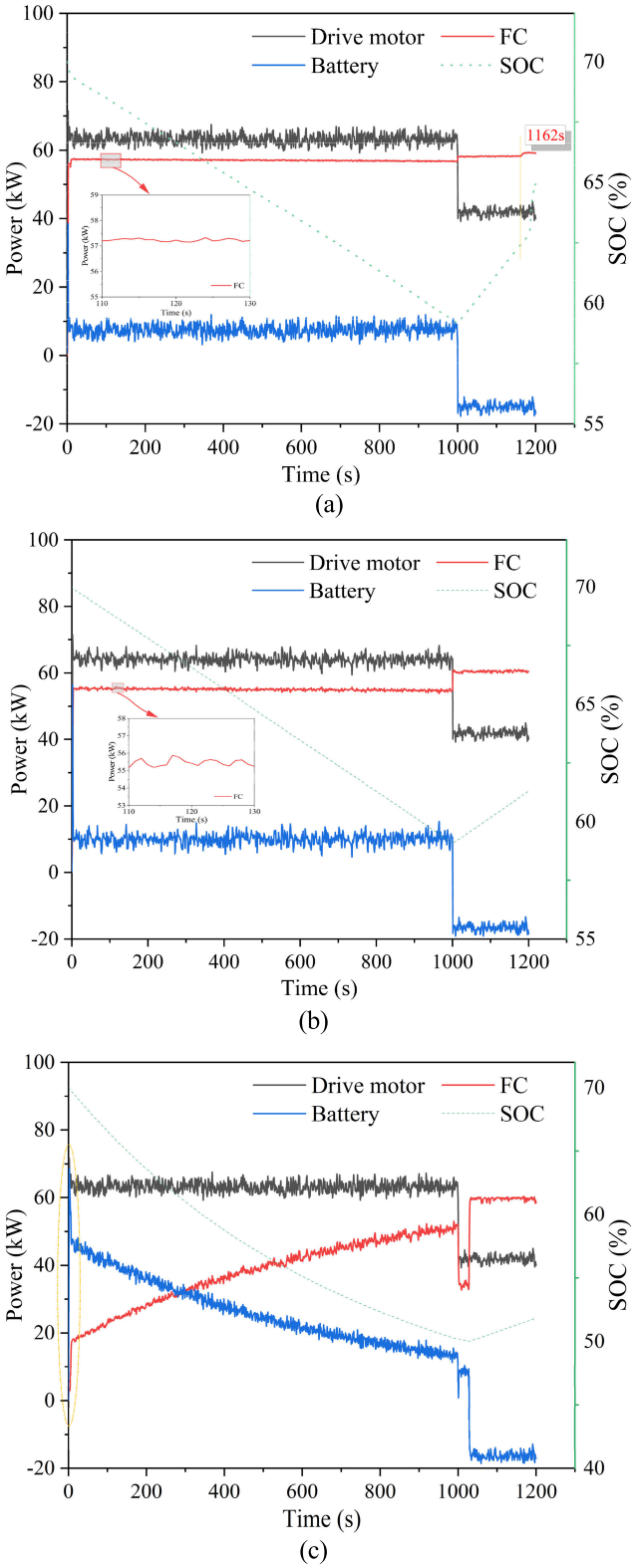

FIGURE 23. The output power of each energy source under three energy management strategies (EMSs) (a) DP; (b) HDP; (c) PF.

In particular, under the DP strategy, in order to meet the specified condition where $SOC_T = SOC_N = 0.65$, a notable increase in FC's output power is observed at the 1162s. Under

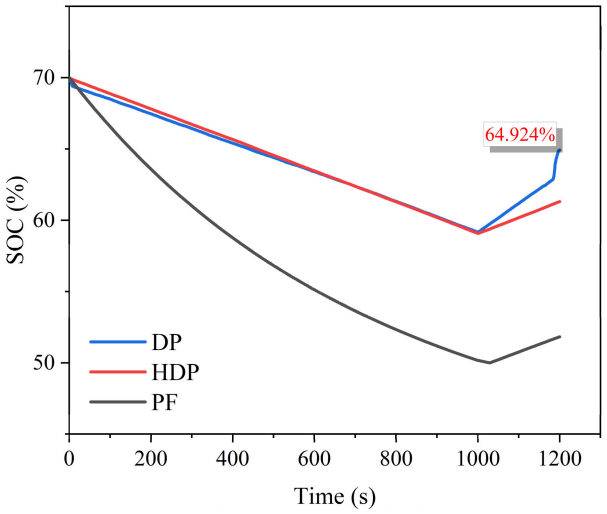

FIGURE 24. The state of charge (SOC) changes under the three strategies.

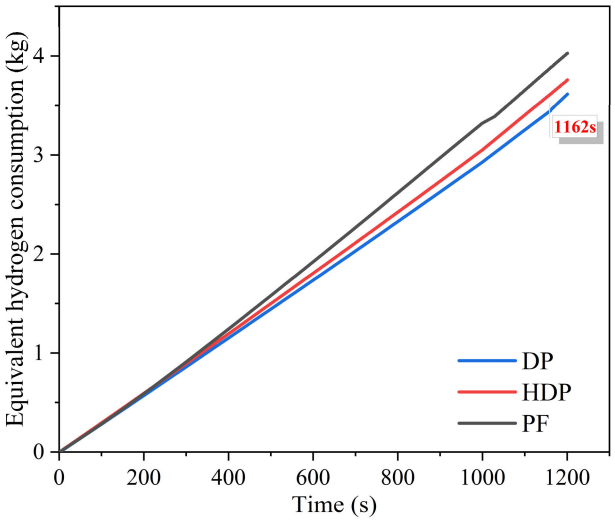

FIGURE 25. The cumulative consumption changes of equivalent hydrogen fuel under the three EMSs.

the PF strategy, before reaching 1000 seconds, $SOC_{\min} < SOC < SOC_{\max}$, there is a gradual increase in the output power of the FC, accompanied by a decrease in the output power of the battery. Between the time interval of 1000 to 1029 seconds, there is a shift in the dynamics. This period is marked by a reduction in the overall load on the vehicle, leading to a simultaneous decrease in both FC and battery output powers. After surpassing the 1029s, $SOC < SOC_{\min}$, The FC not only supplies the required power for the vehicle but also takes on the additional task of charging the battery., which in accordance with the settings specified by the PF strategy.

Figure 24 displays the changes in SOC under three strategies, and Table 6 shows the corresponding SOC results. Upon examining the graph, it becomes evident that the changes in SOC under the DP and HDP strategies closely resemble each

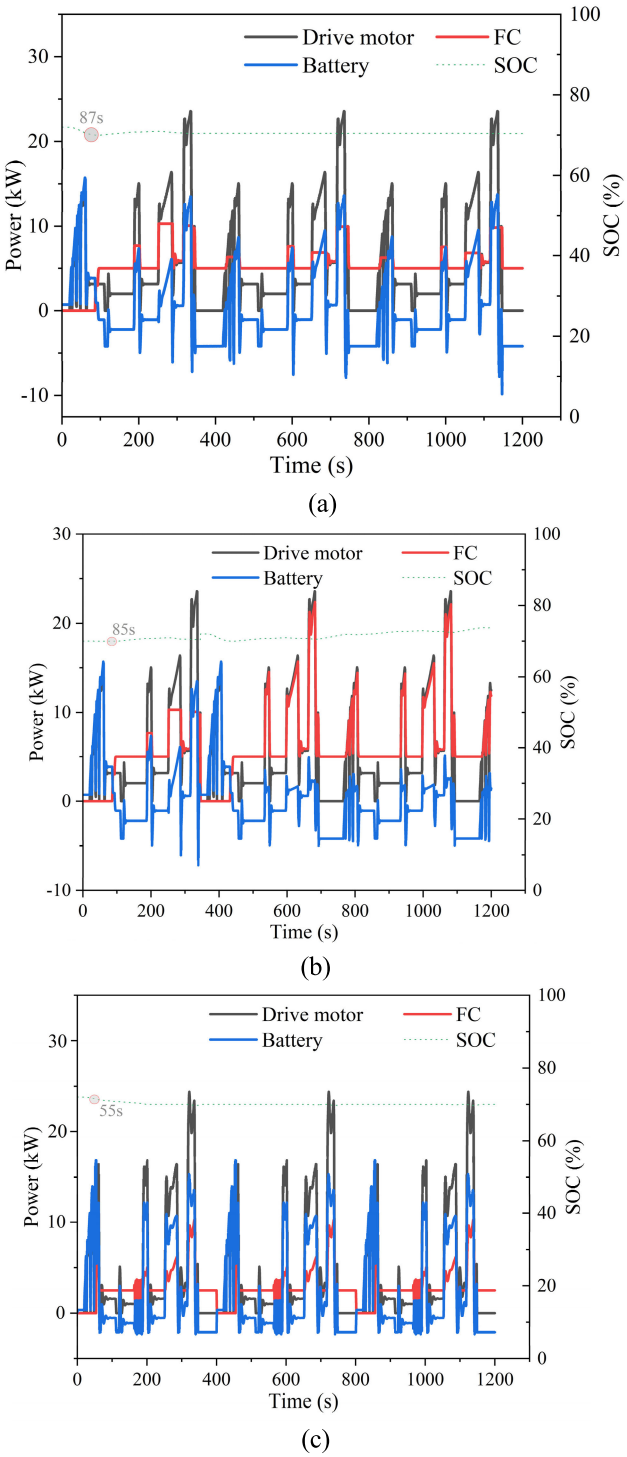

FIGURE 26. The output power of each energy source under three EMSs (a) DP; (b) HDP; (c) PF.

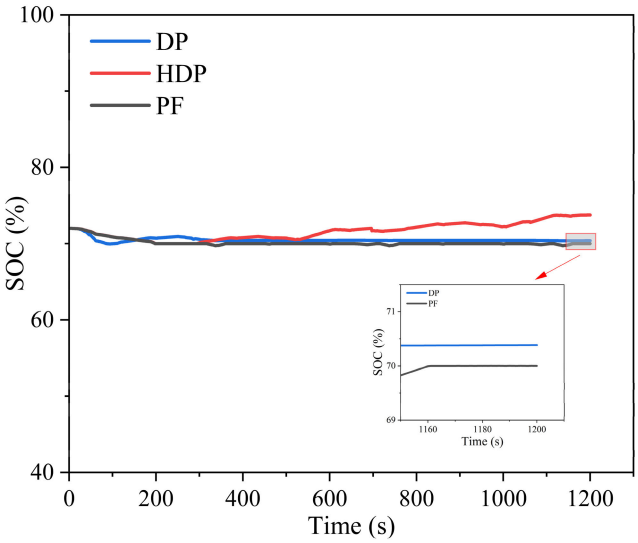

FIGURE 27. The SOC changes under the three strategies.

other during the initial 1000 seconds. However, it is worth noting that DP exhibits a slightly gentler slope compared to HDP, suggesting a smoother discharge pattern for the battery under the DP strategy. Under the DP strategy, after 1162s, to achieve the pre-set value, the discharge power of FC increases. From the DP results, it's evident that and deviate from by 0.075, which is caused by the cumulative error in the energy consumption assessment of batteries. In a longitudinal comparison, the extent of SOC variation is ranked as follows: DP < HDP < PF, relative to the initial value SOC_{IP}.

Figure 25 and Table 7 respectively depict changes and results in the cumulative equivalent hydrogen fuel consumption for the three EMSs. The order of cumulative FC consumption is: PF<DP<HDP. The order of cumulative equivalent hydrogen fuel consumption for battery is: DP< HDP< PF. The order of the equivalent hydrogen consumption from FC and battery is: DP< HDP< PF. As a result, under the PF strategy, the FC has the lowest utilization rate, while the battery has the highest utilization rate. This strategy does not effectively harness the FC to maximize zero emissions and somewhat shortens the lifespan of battery. Due to slightly larger FC power fluctuations under HDP compared to DP, the FC hydrogen consumption is slightly higher than DP. In a longitudinal comparison, compared with PF, the equivalent hydrogen consumption of DP and HDP decreased by 10.278% and 6.728%, respectively.

2) TRANSPORTATION CONDITION

To better reflect real-world driving conditions and extend the duration of transportation condition, the transportation condition is simulated three times for repetition during the optimization process.

Figure 26 illustrates the power output of various energy sources for the HFCT across three EMSs. With an initial SOC set at 72%, the entire power demand is initially borne by the battery until the SOC decreased to 70%. Specifically, under the PF strategy, the battery carried a higher load of the tractor demanded power than the FC, leading to an underutilization of the fuel cell as the primary energy source and a reduction in the lifespan of the battery. In the DP strategy, the FC exhibited the most stable power output, thereby safeguarding the

TABLE 6. The SOC results for the three strategies under ploughing condition.

Strategy	SOC_{IP}	SOC_{FP}	SOC_T	$\Delta SOC_1 = \lvert SOC_{FP} - SOC_T \rvert$	$\Delta SOC_2 = \lvert SOC_{IP} - SOC_T \rvert$
DP	70%	65%	64.925%	0.075%	5.075%
HDP	70%	65%	61.304%	3.696%	8.696%
PF	70%	65%	51.826%	13.174%	18.174%

TABLE 7. Hydrogen fuel consumption results under ploughing condition.

Strategy	Cumulative hydrogen consumption of FC (kg)	Cumulative equivalent hydrogen consumption of battery (kg)	Equivalent hydrogen consumption of energy system (kg)
DP	3.167	0.447	3.614
HDP	3.191	0.567	3.757
PF	2.420	1.608	4.028

TABLE 8. The SOC results for the three strategies under transportation condition.

Strategy	SOC_{IT}	SOC_{FT}	SOC_T	$\Delta SOC_1 = \lvert SOC_{FP} - SOC_T \rvert$	$\Delta SOC_2 = \lvert SOC_{IP} - SOC_T \rvert$
DP	72%	70%	70.384%	0.384%	1.616%
HDP	72%	70%	73.751%	3.751%	1.751%
PF	72%	70%	70.001%	0.001%	1.999%

TABLE 9. Hydrogen fuel consumption results under transportation condition.

Strategy	Cumulative hydrogen consumption of FC (kg)	Cumulative equivalent hydrogen consumption of battery (kg)	Equivalent hydrogen consumption of energy system (kg)
DP	0.506	0.097	0.603
HDP	0.621	0.062	0.683
PF	0.513	0.205	0.718

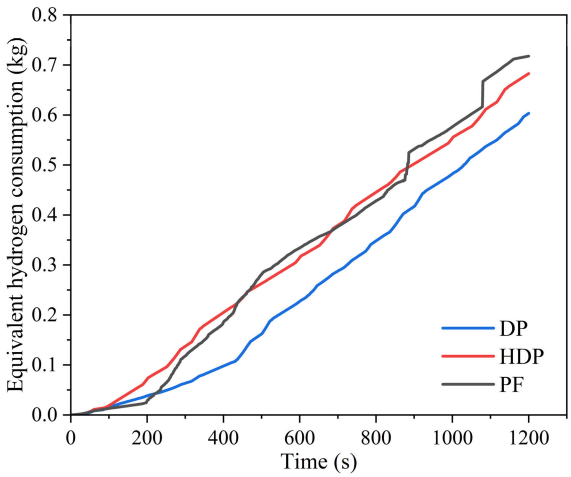

FIGURE 28. The cumulative consumption changes of equivalent hydrogen fuel under the three EMSs.

lifespan of both the FC and the battery. In the HDP strategy, the FC efficiently provided the primary power demand for the tractor in its high-efficiency zone, maximizing the utilization of the FC.

Fig. 27 illustrates SOC changes under three strategies, and Table 8 presents the SOC outcomes. Notably, the DP strategy exhibits the smoothest SOC variation, closely approaching the target final value SOC_{FT} compared to HDP. The HDP strategy, leveraging the fuel cell extensively, results in a slight SOC increase. In summary, the SOC changes, relative to the initial values, follow the order: DP < HDP < PF.

Fig. 28 and Table 9 show equivalent hydrogen consumption changes and outcomes under three strategies. FC consumption ranks: DP<PF <HDP. Battery consumption order: HDP< DP< PF. The equivalent hydrogen consumption from energy sources order: DP< HDP< PF. Notably, under HDP strategy, FC utilization is highest, DP strategy results in the least hydrogen consumption, and PF strategy, relying on the battery for main power, incurs the highest equivalent hydrogen consumption. Vertically comparing DP and HDP to PF, there are reductions of 16.02% and 4.87%, respectively, in equivalent hydrogen consumption.

V. CONCLUSION

This paper presents a comprehensive approach that encompasses the entire process of system design, optimization, and

validation for a HFCT with a fuel cell/battery hybrid energy system.

1) This study focuses on HFCT utilizing the FC and battery as the energy system. Following tractor design principles and employing a general modeling approach based on BG, the powertrain system for HFCT is developed, and a machine-electric-hydraulic integrated power BGM is constructed in the 20-sim simulation software environment, which includes the energy system, drive system, and lifting system. Furthermore, rapid interaction between 20-sim and Matlab/Simulink software is achieved.
2) In the realm of FC/ battery energy system, a HDP algorithm is introduced. The upper layer produces DP power allocation results. The lower layer employs the GRNN algorithm to learn from the DP outputs and applies MIV preprocessing to the input variables. This method resolves the real-time application challenge faced by DP and reduces training time.
3) Employing the V-model rapid development framework in conjunction with field test plowing condition data and the designed transportation condition, a Matlab-HIL test platform is established. The platform, comprising 20-sim, Matlab/Simulink, HIL cabinet, and PowerECU-57A control unit, served as the core hardware and software components. Through MIL and HIL validation processes, the accuracy and superiority of both the HFCT model and the EMS are confirmed.
4) The simulation results demonstrated that the designed tractor simulation model and EMS model exhibited correctness and superiority. In plowing conditions, the DP and HDP strategies exhibited reductions of 10.278% and 6.728%, respectively, in equivalent hydrogen consumption compared to PF strategy. In transportation conditions, the reductions are 16.02% for DP strategy and 4.87% for HDP strategy, both relative to PF strategy.

The findings of this research offer theoretical backing for the modeling and optimization of energy management in the HFCT. Furthermore, they offer certain insights for the development of low-carbon modern agricultural machinery.

ACKNOWLEDGMENT

The authors would like to thank the anonymous reviewers for providing critical comments and suggestions that improved the manuscript.

REFERENCES

[1] R. Zhang and H. Gao, "Analysis of trend of diesel oil consumption of agricultural mechanization and energy-saving strategic measures in China," *Trans. Chin. Soc. Agricult. Eng.*, vol. 23, pp. 280–284, Dec. 2007, doi: 10.3321/j.issn:1002-6819.2007.12.053.

[2] M. Liu, S. Lei, J. Zhao, Z. Meng, C. Zhao, and L. Xu, "Review of development process and research status of electric tractors," *Trans. Chin. Soc. Agricult. Machinery*, vol. 53, pp. 348–364, Nov. 2022, doi: 10.6041/j.issn.1000-1298.2022.S1.039.

[3] M. Liu, "Study on design theory and control strategy of electric tractor," Ph.D. dissertation, Dept. Mech. Eng., Xi'an Univ. Technol., Xi'an, China, 2020.

[4] L. Xu, M. Liu, and Z. Zhou, "Design of drive system for series hybrid electric tractor," *Trans. Chin. Soc. Agricult. Eng.*, vol. 30, pp. 11–18, May 2014, doi: 10.3969/j.issn.1002-6819.2014.09.002.

[5] J. Zhang, G. Feng, L. Xu, W. Wang, X. Yan and M. Liu, "Energy-saving control of hybrid tractor based on Pontryagin's minimum principle," *Trans. Chin. Soc. Agricult. Machinery.*, vol. 54, pp. 396–406, May 2023, doi: 10.6041/j.issn.1000-1298.2023.05.041.

[6] Z. Zhu, Y. Yang, D. Wang, Y. Cai, and L. Lai, "Energy saving performance of agricultural tractor equipped with mechanic-electronic-hydraulic powertrain system," *Agriculture*, vol. 12, no. 3, p. 436, Mar. 2022, doi: 10.3390/agriculture12030436.

[7] F. Tao, L. Zhu, Z. Fu, P. Si, and L. Sun, "Frequency decoupling-based energy management strategy for fuel cell/battery/ultracapacitor hybrid vehicle using fuzzy control method," *IEEE Access*, vol. 8, pp. 166491–166502, 2020, doi: 10.1109/ACCESS.2020.3023470.

[8] W. Xu, M. Liu, L. Xu, and S. Zhang, "Energy management strategy of hydrogen fuel cell/battery/ultracapacitor hybrid tractor based on efficiency optimization," *Appl. Sci.*, vol. 13, no. 1, p. 151, Dec. 2022, doi: 10.3390/app13010151.

[9] Y. Sun, "Study on energy management of pure electric tractor based on super capacitor auxiliary," M.S. thesis, Dept. Vehicle Eng., Jiangsu Univ., Jiangsu, China, 2018.

[10] R. Quan, C. Wang, F. Wu, Y. Chang, and Y. Deng, "Parameter matching and optimization of an ISG mild hybrid powertrain based on an automobile exhaust thermoelectric generator," *J. Electron. Mater.*, vol. 49, no. 5, pp. 2734–2746, May 2020, doi: 10.1007/s11664-019-07680-y.

[11] D. Li, B. Xu, J. Tian, and Z. Ma, "Energy management strategy for fuel cell and battery hybrid vehicle based on fuzzy logic," *Processes*, vol. 8, no. 8, p. 882, Jul. 2020, doi: 10.3390/pr8080882.

[12] H.-S. Lee, J.-S. Kim, Y.-I. Park, and S.-W. Cha, "Rule-based power distribution in the power train of a parallel hybrid tractor for fuel savings," *Int. J. Precis. Eng. Manuf.-Green Technol.*, vol. 3, no. 3, pp. 231–237, Jul. 2016, doi: 10.1007/s40684-016-0030-6.

[13] Y. Li, Li. L, Tian. J, K. Yuan, and Y. Chen, "Energy control strategy of electric tractor power supply based on dynamic programming," *Trans. Chin. Soc. Agricult. Machinery*, vol. 51, pp. 403–410, Apr. 2020, doi: 10.6041/j.issn.1000-1298.2020.04.047.

[14] C. Wang, "Design and research of power system of fuel cell tractor," M.S. thesis, Dept. Mech. Eng., Hubei Univ. Technol., Hubei, China, 2020.

[15] H. Yang, Y. Sun, C. Xia, and H. Zhang, "Research on energy management strategy of fuel cell electric tractor based on multi-algorithm fusion and optimization," *Energies*, vol. 15, no. 17, p. 6389, Sep. 2022, doi: 10.3390/en15176389.

[16] V. Martini, F. Mocera, and A. Somà, "Numerical investigation of a fuel cell-powered agricultural tractor," *Energies*, vol. 15, no. 23, p. 8818, Nov. 2022, doi: 10.3390/en15238818.

[17] L. Xu, E. Liu, M. Liu, X. Zhao and T. Wang, "Energy management strategy of fuel cell/battery hybrid power electric tractor," *J. Henan Univ. Sci. Technol. Natural Sci.*, vol. 40, pp. 80–86, Apr. 2019, doi: 10.15926/j.cnki.issn1672-6871.2019.02.015.

[18] M. Liu, Y. Li, L. Xu, Y. Wang, and J. Zhao, "General modeling and energy management optimization for the fuel cell electric tractor with mechanical shunt type," *Comput. Electron. Agricult.*, vol. 213, Oct. 2023, Art. no. 108178, doi: 10.1016/j.compag.2023.108178.

[19] Y. Huangfu, C. Tian, S. Zhuo, L. Xu, P. Li, S. Quan, Y. Zhang, and R. Ma, "An optimal energy management strategy with subsection bi-objective optimization dynamic programming for photovoltaic/battery/hydrogen hybrid energy system," *Int. J. Hydrogen Energy*, vol. 48, no. 8, pp. 3154–3170, Jan. 2023, doi: 10.1016/j.ijhydene.2022.10.133.

[20] H. Zhang, "Research on energy management for fuel cell hybrid tramway," Ph.D. dissertation, Dept. Traffic Inf. Eng. Control, Southwest Jiaotong Univ., Chengdu, China, 2021, doi: 10.27414/d.cnki.gxnju.2021.000082.

[21] H. Gu, B. Yin, Y. Yu, and Y. Sun, "Energy management strategy considering fuel economy and life of fuel cell for fuel cell electric vehicles," *J. Energy Eng.*, vol. 149, no. 1, Feb. 2023, Art. no. 04022054, doi: 10.1061/(asce)ey.1943-7897.0000871.

[22] R. Pan, "Research on aging behavior modeling and lifespan prolongation strategy of fuel cell with external characteristics," Ph.D. dissertation, Dept. Control Sci. Eng., Univ. Sci. Technol. China, Anhui, China, 2020, doi: 10.27517/d.cnki.gzkju.2020.000345.

[23] K. Song, Y. Wang, C. An, H. Xu, and Y. Ding, "Design and validation of energy management strategy for extended-range fuel cell electric vehicle using bond graph method," *Energies*, vol. 14, no. 2, p. 380, Jan. 2021, doi: 10.3390/en14020380.
[24] W. Xiong, G. Bao, and H. Li, "20-sim software introduction and application," *Chin. Hydraul. Pneumatics.*, vol. 4, pp. 31–33, Dec. 2000.
[25] E. Chen and J. Tang, "Bond graph modeling and dynamic simulation of damper test-Bed' hydraulic system based on 20-sim software," *J. Eng. Des.*, vol. 17, no. 5, pp. 339–344, Oct. 2010, doi: 10.3785/j.issn.1006-754X.2010.05.005.
[26] (2013). *20-Sim 4.4 Reference Manual*. [Online]. Available: https://www.20sim.com/downloads/files/20simReference44.pdf
[27] L. Xu, "Study on characteristics of hydro-mechanical continuously variable transmission of tractor," Ph.D. dissertation, Dept. Vehicle Eng., Xi'an Univ. Technol., Xi'an, China, 2007.
[28] H. Chen, J. Chen, Z. Liu, and H. Lu, "Real-time optimal energy management for a fuel cell/battery hybrid system," *Asian J. Control*, vol. 21, no. 4, pp. 1847–1856, Jul. 2019, doi: 10.1002/asjc.2065.
[29] S. Onori, L. Serrao, and G. Rizzoni, *Hybrid Electric Vehicles: Energy Management Strategies*. New York, NY, USA: Springer, 2015.
[30] L. Xu, J. Li, J. Hua, X. Li, and M. Ouyang, "Adaptive supervisory control strategy of a fuel cell/battery-powered city bus," *J. Power Sources*, vol. 194, no. 1, pp. 360–368, Oct. 2009, doi: 10.1016/j.jpowsour.2009.04.074.
[31] Y. Liu, J. Liang, J. Song, and J. Ye, "Research on energy management strategy of fuel cell vehicle based on multi-dimensional dynamic programming," *Energies*, vol. 15, no. 14, p. 5190, Jul. 2022, doi: 10.3390/en15145190.
[32] Y. Liu, Z. Chen, and Y. Zhang, *Energy Management and Optimization Strategies for New Energy Vehicles*. Chongqing, China: Chongqing Univ. Press, 2021.
[33] L. Yu, *MATLAB Intelligent Algorithm 30 Case Analysis*. Beijing, China: Beihang Univ. Press, 2015.
[34] H. Du, "Hierarchical energy management strategy of composite energy storage fuel cell vehicle based on energy source equal life design," M.S. thesis, Dept. Vehicle Eng., Chongqing Univ., Chongqing, China, 2022.
[35] Y. Zhou, "Research on rolling bearing fault diagnosis technology based on MIV feature screening and BP neural network," M.S. thesis, Dept. Mech. Manuf. Automat., Beijing Jiaotong Univ., Beijing, China, 2011.
[36] X. Yan, Z. Zhou, and Z. Li, "Study on the noise reduction of tractor power take-off load by empirical mode decomposition soft-threshold method," *J. Xi'an Jiaotong Univ.*, vol. 53, no. 5, pp. 67–72, May 2019, doi: 10.7652/xjtuxb201905010.
[37] F. Qin, G. Xu, Y. Hu, K. Xu, and W. Li, "Stochastic optimal control of parallel hybrid electric vehicles," *Energies*, vol. 10, no. 2, p. 214, Feb. 2017, doi: 10.3390/en10020214.
[38] T. Liu, Y. Zou, D. Liu, and F. Sun, "Reinforcement learning of adaptive energy management with transition probability for a hybrid electric tracked vehicle," *IEEE Trans. Ind. Electron.*, vol. 62, no. 12, pp. 7837–7846, Dec. 2015, doi: 10.1109/TIE.2015.2475419.

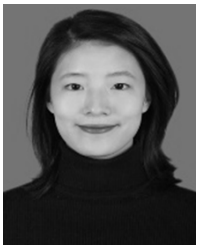

YANYING LI (Member, IEEE) received the B.S. and M.S. degrees from the Henan University of Science and Technology, Luoyang, China, in 2019 and 2022, respectively, where she is currently pursuing the Ph.D. degree. Her research interests include novel drivetrain and intelligent control technology for agricultural tractors.

MENGNAN LIU (Member, IEEE) received the Ph.D. degree from the Xi'an University of Technology in 2021. He is currently the Product Management Director with the First Tractor Company Ltd. In the meantime, he is also the Deputy Director at the State Key Laboratory of Intelligent Agricultural Power Equipment, as a Senior Engineer at the professor level, he holds the position of Ph.D. Supervisor at the Henan University of Science and Technology. His main research interests include encompass novel drivetrain and intelligent control technology for agricultural machinery.

YITING WANG received the B.S. degree from the College of Vehicle and Traffic Engineering, Henan University of Science and Technology, Luoyang, China, in 2021, where she is currently pursuing the M.S. degree. Her research interests include novel drivetrain and intelligent control technology for agricultural tractors.

LIYOU XU (Member, IEEE) received the B.S. degree in mechanical manufacturing technology and equipment from the Luoyang Institute of Technology, Jiaozuo, China, in 1998, the Ph.D. degree in vehicle engineering from the Xi'an University of Technology, Xi'an, in 2007, and the M.S. degree in vehicle engineering from the Luoyang Institute of Technology, Luoyang, China, in 2018. Since 2013, he has been a Professor with the College of Vehicle and Traffic Engineering, Henan University of Science and Technology, Luoyang, China. His research interests include new transmission theory and control technology, vehicle encompass analysis method and simulation technology, and low-speed electric vehicle transmission technology.

SHENGHUI LEI received the M.S. degree from the College of Vehicle and Traffic Engineering, Henan University of Science and Technology, Luoyang, China, in 2022, where he is currently pursuing the Ph.D. degree. His research interests include novel drivetrain and intelligent control technology for agricultural tractors.